Journal of the Meteorological Society of Japan

EARLY ONLINE RELEASE

The DOI for this manuscript is
DOI:10.2151/jmsj.2024-028
J-STAGE Advance published date: May 28th, 2024
The final manuscript after publication will replace the preliminary version at the above DOI once it is available.

How do the tropics precipitate? Daily variations in precipitation and cloud distribution

Hans Segura

Max Planck Institute for Meteorology, Hamburg, Germany

and

Cathy Hohenegger

Max Planck Institute for Meteorology, Hamburg, Germany

May 10, 2024

Corresponding author: Hans Segura, Max Planck Institute for Meteorology, Bundesstrasse 53, 20146 Hamburg, Germany.
E-mail: hans.segura@mpimet.mpg.de

Abstract

What controls the variability of daily precipitation averaged over the tropics? Are these the most numerous precipitation rates or the most intense ones? And do they relate to a specific cloud type? This work addresses these questions using precipitation from the one-year simulation of the global-coupled storm-resolving ICOsahedral Non-hydrostatic model run in its Sapphire configuration (ICON-Sapphire) and observations. Moreover, we develop a framework to analyze the precipitation variability based on the area covered by and the mean intensity of different groups of precipitation rates. Our framework shows that 60% of the precipitation variability is explained by precipitation rates between 20 and 70 mm d^{-1}, but those precipitation rates only explain 46% of the mean precipitation in the tropics. The decomposition of the precipitation variability into the area fraction and mean intensity of a set of precipitation rates shows that this variability is explained by changes in the area fraction covered by precipitation rates between 20 and 70 mm d^{-1}, not by changes in the mean intensity. These changes in the area fraction result from changes in the area covered by congestus clouds, not by cumulonimbus or shallow clouds, even though congesti and cumulonimbi contribute equally to the mean tropical precipitation.

Overall, ICON-Sapphire reproduces the probability density function of precipitation rates and the control of specific precipitation rates on the tropical

mean precipitation and variability compared to observations.

Keywords global-coupled storm-resolving models; tropical precipitation variability; area fraction of precipitating regions; tropical convective clouds

1. Introduction

According to satellite observations, only 12.5% of the climatological mean precipitation in the tropics comes from precipitation rates greater than 70 mm d^{-1} (Fig. 1b in Zhou et al., 2013). Likewise, only 12.5% comes from precipitation rates smaller than 5 mm d^{-1}, referred to as light precipitation in Sun et al. (2018). That is, neither the most intense nor the most frequent precipitation rates contribute the most to the tropical precipitation mean. On a particular day, the area covered by intense precipitating regions is small, and because the precipitation mean in the tropics depends more on the fractional area than on intensity (Doneaud et al., 1984; Lopez et al., 1989), this explains the minor role played by intense precipitation rates.

Beyond which precipitation rates control the mean tropical precipitation, which precipitation rates control its day-to-day variability? It is logical to think that the precipitation rates explaining most of the precipitation mean also explain most of the day-to-day precipitation variability. However, it is possible to imagine that the amount of water that those precipitation rates bring is similar on a day-to-day basis, and in that case, the variability mostly results from the occurrence of heavy or light precipitation rates. The day-to-day tropical precipitation variability has not been as much studied as the mean. Yet, daily changes in tropical precipitation are related to floods (see Fig. 1 in Berndtsson and Niemczynowicz, 1988) and changes in water reservoirs (see Fig. 1 in Cristiano et al., 2017) with consequences for agriculture (Rowhani et al., 2011; Cabas et al., 2010) and population health (Shively, 2017; Mukabutera et al., 2016). Moreover, the day-to-day variability is supposed to increase more than the mean with climate change (Pendergrass et al., 2017). Thus, understanding whether area or intensity and which precipitation rates control the day-to-day variability in precipitation is important.

This understanding is also crucial for modeling the climate system. State-of-the-art climate models using convective parameterizations are known for simulating too frequent light precipitation rates (Dai, 2006). Even in models using horizontal grid spacing finer than 10 km, the problem persists as long as a convective parameterization is used (Judt and Rios-Berrios, 2021; Ma et al., 2022). This leads to an overestimation of their contribution to the precipitation mean in the region comprised between 50°N and 50°S (Dai, 2006). Using a convective parameterization also leads to an overestimation in the persistence of the day-to-day tropical precipitation (Roehrig et al., 2013; Moon et al., 2019; Fiedler et al., 2020). Precipitation appears more frequent compared to observations in places where precipitation occurred one day before. Just by avoiding the use of a convective parameterization, regional and global atmosphere-only storm-resolving models can get rid of the light precipitation problem (Na et al., 2020; Judt and Rios-Berrios, 2021). This suggests a more correct partitioning of the precipitation mean in its rates, although this hasn't been formally shown yet. Likewise, the factors controlling the day-to-day precipitation variability in storm-resolving models and the realism of these relationships haven't been investigated yet.

The study of the different precipitation rates in the tropics intrinsically links to the study of convective clouds that bring precipitation. There are three groups of convective clouds in this category: shallow, congestus, and cumulonimbus clouds (Johnson et al., 1999). Shallow clouds precipitate little or not at all. The high precipitation rates characteristic of cumulonimbus makes them an important contributor to tropical precipitation (Cheng and Houze, 1979; Rickenbach and Rutledge, 1998; Johnson et al., 1999). Originally, cumulonimbus and shallow clouds were the two categories of tropical clouds, but this view changed after the results from the Global Atmospheric Research Program Atlantic Tropical Experiment - GATE (Houze and Cheng, 1977; Warner et al., 1980) and the Tropical Ocean Global Atmosphere Coupled Ocean-Atmosphere Response TOGA- COARE (Rickenbach and Rutledge, 1998; Johnson et al., 1999) field campaigns. Both campaigns noticed clouds populating the mid-troposphere with tops reaching the freezing level, i.e., congestus clouds. While the precipitation rates of congestus are lower than those of cumulonimbus, congestus clouds contributed up to 25% of the total precipitation from organized storms and up to 52% of the total precipitation from individual cells during TOGA-COARE (Johnson et al., 1999). Hence, cumulonimbus and congestus clouds are the main contributors to the tropical precipitation mean, yet it is still unknown whether the day-to-day variability of precipitation in the tropics is related to a certain type of cloud.

We aim to determine in this study whether certain precipitation rates control the day-to-day variation of the time series of precipitation averaged over the tropics. The identification of these particular precipitation rates allows us to formally isolate the contribution from changes in precipitating area fraction and in precipitation intensities, as well as to which type of convective clouds (shallow, congestus, or cumulonimbus) they belong. We also investigate whether the same precipitation rates can explain both the mean and its variability. To reach our goal, we take advantage of the global-coupled storm-resolving ICOsahedral Non-hydrostatic (ICON) model with a horizontal grid spacing of 5km and integrated with its Sapphire configuration (Hohenegger et al., 2023) as well as of observations. Our intention in using a model simulation and observations is to identify if the relationships between tropical precipitation and its probability density function of precipitation rates are similar in model and observation despite the presence of precipitation biases in ICON. Moreover, by analyzing the type of tropical cloud explaining the variability of precipitation, we also validate the representation of convective clouds in ICON, for the first time using a global-coupled storm-resolving model.

The structure of this manuscript is as follows. Section 2 describes ICON with the configuration used in this study and the observational data set. We also describe the methodology used to classify tropical clouds in ICON. In Section 2, we also explain the framework developed to analyze the variability of tropical precipitation in terms of intensity and area fraction of precipitating regions. We present in section 3 the probability distribution function of the precipitation rates in ICON and observations and their contribution to the tropical precipitation mean. In section 4, we identify the precipitation rates influencing the tropical precipitation variability, as well as the role of the area fraction and intensity. Section 5 addresses the distribution of tropical clouds and identifies the type of cloud accompanying the variability of tropical precipitation. The main conclusions of our study are provided in section 6.

2. Methods

2.1 Model

a. ICON

We make use of the global-coupled storm-resolving model ICON integrated with the Sapphire configuration and with a horizontal grid spacing of 5km. ICON, with this configuration, targets to represent processes of the Climate System at kilometer scales, e.g., meso-beta scale processes in the atmosphere and mesoscale ocean eddies. We use the simulation G_AO_5 km, described in Hohenegger et al. (2023). It is referred to in this study as ICON-Sapphire. In this simulation, the atmosphere is discretized in 90 vertical levels, the ocean in 128 vertical levels, and the land in five soil layers. ICON-Sapphire is integrated for one year, from February 1, 2020, to January 31, 2021, and we analyze precipitation and clouds in the tropics (30°S-30°N) from this one-year simulation. We compute the daily average of the precipitation flux, with units kg m^{-2} s^{-1}, from 30-minute mean output on the native grid of ICON. Then, the precipitation field is scaled to match the units of mm d^{-1} and horizontally interpolated using a conservative method to a regular lat-lon grid of 0.1° x 0.1°. For the analysis of clouds, we use the 3D-variable cloud liquid water content (q_l) on the native grid, daily averaged from 6-hourly instantaneous output. We also use precipitation in the native grid of ICON to analyze the contribution of the tropical clouds to the mean and day-to-day variability of precipitation in the tropics.

b. *Classification of clouds in ICON-Sapphire*

We classify tropical clouds in ICON-Sapphire based on the cloud top and base height. Using daily means values of q_l, we identify in each grid cell the maximum altitude where the value of 0.01 g kg^{-1} is located. This altitude is considered as being the cloud top height (CTH). We also calculate the cloud base height (CBH) by identifying the minimum altitude where q_l is greater than 0.01 g kg^{-1}. Over land, the altitude of the terrain is subtracted from CBH and CTH. Then, we select only clouds with a CBH of less than 3 km. Next, we categorize clouds into three groups depending on CTH: low-level clouds, for CTH below 4 km, congestus for clouds with a CTH between 4 and 8 km, and cumulonimbus for clouds with a CTH between 8 and 15 km.

In our analysis, we compute the area that each type of cloud covers for the tropics. For this, we count the number of grid points in which a cloud type is identified in the entire tropics and throughout the 366 days of analysis. This number is divided by the total number of data, which is the total number of grid points in the tropics times 366 days. This means that for the area covered, we refer to the relative frequency in time and space. The space could be the entire tropics, as explained before, or could be restricted to an area where grid points precipitate in a certain range. The contribution to the total amount of precipitation in the tropics for each type of cloud is also calculated. In this case, the precipitation for each grid point identified with a type of cloud is added across the tropics and the 366 days of analysis. Then, this number is divided by the total amount of water falling in the tropics during the 366 days of analysis.

2.2 Satellite precipitation

Together with ICON-Sapphire, we also use the Integrated Multi-SatellitE Retrievals for GPM (IMERG) version 06 (Huffman et al., 2019) to analyze tropical precipitation on a daily time step. The period of the analysis is similar to ICON-Sapphire, from February 1, 2020, to January 31, 2021. The horizontal resolution of IMERG is 0.1° x 0.1°.

2.3 Derivation of day-to-day precipitation variability

To analyze the day-to-day variability of tropical precipitation (also referred to hereafter as tropical precipitation variability), we follow the framework introduced by Atlas et al. (1990). We start by calculating the yearly mean and tropically averaged precipitation from individual daily precipitation rates $\overline{[P]}_{\tau}^{\tau+\delta\tau}$

$$\overline{[P]}_{\tau}^{\tau+\delta\tau} = \frac{\int_{t=1}^{t=366} \langle P(\lambda,\phi,t) A_{\tau}^{\tau+\delta\tau}(\lambda,\phi,t) \rangle \, dt}{\langle A_{\tau=0}^{\tau=\infty}(\lambda,\phi) \rangle \int_{t=1}^{t=366} \, dt} \tag{1}$$

The term on the left-hand side indicates the yearly mean tropical precipitation of precipitation rates between τ and $\tau+\delta\tau$ (e.g., between 0.1 and 1 mm d^{-1}). The summing of $\overline{[P]}_{\tau}^{\tau+\delta\tau}$ using all the precipitation rates gives the yearly tropical mean precipitation $\overline{[P]}$. The operator $[\ \ ]$ and $\overline{}$ indicate the average in space and time t, respectively. The time discretization is daily. On the righ-hand side, the operator $\langle\rangle$ indicates tropical summation defined by: $\langle\ \ \rangle = \int_{-180}^{180} \int_{-30}^{30} .. \cos\phi \, d\phi \, d\lambda$. λ and ϕ are longitude and latitude, respectively. P is the grid-point precipitation rate, and $A_{\tau}^{\tau+\delta\tau}$ is a mask that takes the values of one (1) for grid points where $\tau \leq P(\lambda,\phi,t) \leq \tau+\delta\tau$ and zero (0) otherwise. In this study, we integrate in time Equation 1 from February 2020 to January 2021.

Using Equation 1, the daily precipitation mean averaged over the tropics from precipitation rates between a certain threshold τ and a precipitation rate close to infinity $[P(t)]_{\tau}^{\infty}$ is:

$$[P(t)]_{\tau}^{\infty} = \frac{\langle P(\lambda,\phi,t) A_{\tau}^{\infty}(\lambda,\phi,t) \rangle}{\langle A_{0}^{\infty}(\lambda,\phi,t) \rangle} \tag{2}$$

or

$$[P(t)]_{\tau}^{\infty} = \frac{\langle A_{\tau}^{\infty}(\lambda,\phi,t) \rangle}{\langle A_{0}^{\infty}(\lambda,\phi,t) \rangle} \frac{\langle P(\lambda,\phi,t) A_{\tau}^{\infty}(\lambda,\phi,t) \rangle}{\langle A_{\tau}^{\infty}(\lambda,\phi,t) \rangle} \tag{3}$$

where $\frac{\langle A_\tau^\infty(\lambda,\phi,t)\rangle}{\langle A_0^\infty(\lambda,\phi,t)\rangle}$ is the area fraction covered by precipitation rates greater than τ, denoted by $\alpha_\tau^\infty(t)$. The term $\frac{\langle P(\lambda,\phi,t)A_\tau^\infty(\lambda,\phi,t)\rangle}{\langle A_\tau^\infty(\lambda,\phi,t)\rangle}$ is the mean intensity of precipitation rates greater than τ and denoted by $I_\tau^\infty(t)$. If τ is equal to zero, Equation 3 gives the daily precipitation averaged over the tropics$[P(t)]$, which can be computed also as:

$$[P(t)] = \alpha_0^\tau(t)I_0^\tau(t) + \alpha_\tau^\infty(t)I_\tau^\infty(t) \tag{4}$$

Moreover,

$$\alpha_0^\tau(t) + \alpha_\tau^\infty(t) = 1 \tag{5}$$

$$I_\tau^\infty(t) - I_0^\tau(t) = \Delta I(t) \tag{6}$$

Introducing Equations 5 and 6 in Equation 4, we obtain:

$$[P(t)] = I_0^\tau(t) + \alpha_\tau^\infty(t)\Delta I(t) \tag{7}$$

Decomposing the terms in Equation 7 in their day-to-day variation $(')$ and their mean state or time mean $(\overline{})$, we can get the following expression for the tropical precipitation variability $[P(t)]'$:

$$[P(t)]' = I_0^\tau(t)' + \alpha_\tau^\infty(t)'\overline{\Delta I} + \Delta I(t)'\overline{\alpha_\tau^\infty} + \alpha_\tau^\infty(t)'\Delta I(t)' - \overline{\alpha_\tau^\infty(t)'\Delta I(t)'} \tag{8}$$

All the terms in the right-hand side of Equation 8 are time series depending on τ. According to this equation, the tropical precipitation variability $[P(t)]'$ is explained by terms having a time-dependent component, which are four ($I_0^\tau(t)'$, $\alpha_\tau^\infty(t)'\overline{\Delta I}$, $\Delta I(t)'\overline{\alpha_\tau^\infty}$ and $\alpha_\tau^\infty(t)'\Delta I(t)'$). The last term, $\overline{\alpha_\tau^\infty(t)'\Delta I(t)'}$ is a constant for a given time series. Thus, Equation 8 indicates that an increase in the tropically averaged precipitation on a given day can be explained by the strengthening of the mean intensity in the less rainy region ($I_0^\tau(t)' > 0$), or the expansion of the more rainy region ($\alpha_\tau^\infty(t)' > 0$), or the intensification in the difference in the mean intensity between the two regions ($\Delta I(t)' > 0$) or if an expansion or shrinking of the region with precipitation rates greater than τ implies an intensification or weakening in the difference of the mean intensity between the two regions, respectively ($\alpha_\tau^\infty(t)'\Delta I(t)' > 0$).

To evaluate Equation 8 we need to discretize precipitation in its rate, and this is computed as follows. The first bin contains precipitation rates below 0.1 mm d^{-1} and the second bin from 0.1 to 1 mm d^{-1}. The range of the bin ($\delta\tau$) is 1,5,10 and 25 mm d^{-1} for precipitation rates from 1 to 5 mm d^{-1}, from 5 to 50 mm d^{-1}, from 50 to 100 mm d^{-1}, and from 100 to 300 mm d^{-1}, respectively. This bin distribution is also used to evaluate Equation 1. Changing the bin size does not change our result regarding the precipitation variability and the similarity between ICON-Sapphire and IMERG in the precipitation frequency. The shape of the distribution regarding the contribution from individual precipitation rates to the tropically averaged precipitation is similar between ICON-Sapphire and IMERG, even if this shape changes with the discretization of precipitation rates (not shown).

3. Mean tropical precipitation

The distribution of precipitation rates in the tropics from ICON-Sapphire and IMERG is displayed in Fig. 1a. ICON-Sapphire matches adequately the distribution of light precipitation rates (<5 mm d^{-1}) with no overestimation visible, confirming the results of global atmospheric-only storm-resolving simulations (Na et al., 2020; Judt and Rios-Berrios, 2021). However, precipitation rates greater than 110 mm d^{-1} occur less frequently in ICON-Sapphire than in IMERG. While at first, it could suggest a bias in the simulation, IMERG also has problems in measuring extreme precipitation events over land (Da Silva et al., 2021; Fang et al., 2019; Zhang et al., 2019) and ocean (Wen et al., 2018). Fig. 1

Now, let's focus on the yearly and tropically averaged precipitation from individual precipitation rates $\overline{[P]}_{\tau}^{\tau+\delta\tau}$ displayed in Fig. 1b and calculated using Equation 1. ICON-Sapphire and IMERG show a similar partitioning of the precipitation mean in its precipitation rates (Fig. 1b). Both data sets indicate low values of mean precipitation from precipitation rates greater than 100 mm d^{-1}. Indeed, the contribution of precipitation rates greater than 100 mm d $^{-1}$ to the overall mean precipitation is small (12.5%; Fig. 1c). This minders the effect of their underestimation in ICON-Sapphire compared to observations on the tropical mean. Besides, 70% of the precipitation mean comes from precipitation rates between 5 and 70 mm d^{-1} in both ICON-Sapphire and IMERG, indicating again the low contribution of very intense precipitation rates. Thus, the partitioning of tropical precipitation in its different precipitation rates is reproduced in ICON-Sapphire, giving us the confidence to tackle the next question: which precipitation rates contribute the most to the day-to-day precipitation variability?

4. Daily tropical precipitation variability

The day-to-day precipitation variability is investigated using Equation 8. The term $\overline{\alpha_{\tau}^{\infty}(t)'\Delta I(t)'}$ in Equation 8 is constant in time, and therefore, cannot explain the tropical precipitation variability, leaving the other four terms as the main contributors. To address the question of whether there is only one term or several terms explaining the tropical precipitation variability, we conduct a correlation analysis between the time series of $[P(t)]'$ and of the four terms for different precipitation thresholds τ, the latter ranging between 0.1 and 300 mm d^{-1}.

Fig. 2 displays this correlation analysis for ICON-Sapphire (Fig. 2a) and IMERG (Fig. 2b). An important feature to highlight in Fig. 2 is the high correlation between $[P(t)]'$ and changes in the area of grid points precipitating more than 20 mm d^{-1} evidenced by the term $\alpha_{20}^{\infty}(t)'\overline{\Delta I}$. The high correlation (r=0.9) is explained by the time-dependent variable $\alpha_{20}^{\infty}(t)'$ because the bar-term $\overline{\Delta I}$ is constant in time. Using the same threshold, the mean intensity of grid points precipitating less than 20 mm d^{-1}, $I_0^{20}(t)'$, or the difference in intensity between the two regions, $\Delta I(t)'\overline{\alpha_{20}^{\infty}}$, show a small correlation coefficient with $[P(t)]'$ in ICON-Sapphire and IMERG. This is also the case for the combined variability of the area fraction of grid points and the difference in intensities between the two regions, $\alpha_{20}^{\infty}(t)'\Delta I(t)'$. $\boxed{\text{Fig. 2}}$

Approaching τ towards infinity has similar influences on the terms explaining $[P(t)]'$ in ICON-Sapphire and IMERG. There is a decrease in the correlation with $\alpha_{\tau}^{\infty}(t)'\overline{\Delta I}$, while the opposite occurs for the mean intensity of precipitation rates less than τ, $I_0^{\tau}(t)'$. However, it is necessary to surpass the threshold of 100 mm d^{-1} to obtain a correlation value similar to the one of $\alpha_{20}^{\infty}(t)'\overline{\Delta I}$. This high correlation value purely results from the fact that $\alpha_0^{100} \approx 1$ leading to $I(t)_0^{100} \approx [P(t)]$ according to Equation 7, and this does not give additional information regarding the variability.

Looking at Fig. 2, the correlation between $[P(t)]'$ and $\alpha_{0.1}^{\infty}(t)'$ shows discrepancies between ICON-Sapphire (r=0.58) and IMERG (r=0.2). Considering that $\alpha_{0.1}^{\infty}(t)' = -\alpha_{0}^{0.1}(t)'$, the following reasoning can explain the difference between ICON-Sapphire and IMERG. An increase in $I_{0}^{0.1}(t)'$ is correlated with a decrease in the number of grid points in the region precipitating less than 0.1 mm d^{-1} ($\alpha_{0}^{0.1}(t)'$) in both, ICON-Sapphire (r=-0.6) and IMERG (r=-0.7). Now in ICON-Sapphire, $\alpha_{0}^{0.1}(t)'$ tends to be anti-correlated (r=-0.45) with $\alpha_{20}^{\infty}(t)'$, whereas this is not the case in IMERG (r=-0.16). Given the high correlation between $[P(t)]'$ and $\alpha_{20}^{\infty}(t)'$, $\alpha_{0.1}^{\infty}(t)'$ and $I_{0}^{0.1}(t)'$ end up highly correlated to $[P(t)]'$ in ICON-Sapphire as well.

But is there an exchange of grid points between the region precipitating more than 20 mm d^{-1} and less than 0.1 mm d^{-1} in ICON-Sapphire? In ICON-Sapphire, new grid points precipitating more than 20 mm d^{-1} tend to come from grid points that were not precipitating before, while they could come from non-precipitating grid points or grid points precipitating more than 0.1 mm d^{-1} in IMERG. The transfers from non-precipitating grid points to strongly precipitating points is confirmed in ICON-Sapphire by summing the positive changes in $\frac{\partial \alpha_{20}^{\infty}(t)'}{\partial t}$ (0.19) for one year and comparing it with the total changes in $\frac{\partial \alpha_{0}^{0.1}(t)'}{\partial t}$ (-0.34) and $\frac{\partial \alpha_{0.1}^{20}(t)'}{\partial t}$ (0.15). These last two are also computed only when $\frac{\partial \alpha_{20}^{\infty}(t)'}{\partial t}$ is positive. This transfer of grid points between non-precipitating and more strongly precipitating regions could be explained by the known spotty nature of precipitation in ICON-Sapphire, explaining why IMERG does not present this relationship. But also the smoothness of the spatial precipitation pattern in IMERG due to the algorithm employed to merge different sources of satellite data (Tan et al., 2016) could prevent IMERG from capturing this relationship. Despite this discrepancy between ICON-Sapphire and IMERG, our results show that the increase or decrease in the number of grid points precipitating more than 20 mm d^{-1}, $\alpha_{20}^{\infty}(t)'\overline{\Delta I}$, and not the intensity of those grid points, explains the variability of the tropical precipitation mean in both data sets. This result is not dependent on the year selected in IMERG nor on the observational data set (Fig. S1). Fig. 3

To confirm that not only the time series of $\alpha_{20}^{\infty}(t)'\overline{\Delta I}$ correlates with $[P(t)]'$, but also matches its variations, we show in (Fig. 3) the time series of the term $[P(t)]'$, $\alpha_{20}^{\infty}(t)'\overline{\Delta I}$, $I_0^{20}(t)'$, $\Delta I(t)'\overline{\alpha_{20}^{\infty}}$ from Eq. 8. The terms $\alpha_0^{20}(t)'\Delta I(t)'$ and $\overline{\alpha_0^{20}(t)'\Delta I(t)'}$ are small enough and are not plotted, but the time series of the six terms can be found in Fig. S2. Visual comparison of the time series (Fig. 3) confirms that the variability in the area fraction of region precipitating more than 20 mm d^{-1} correlates with the precipitation variability, not only on a seasonal time scale but also in the day-to-day variability. Removing the variability larger than 60 days by subtracting the running mean with a 60-day window in $\alpha_{20}^{\infty}(t)'$ and $[P(t)]'$, and recomputing the correlation analysis gives a correlation value of 0.9 in ICON-Sapphire and IMERG (Table 1).

Are intense precipitation rates important?

With thresholds greater than 20 mm d^{-1}, the correlation between $\alpha_\tau^\infty(t)'$ and $[P(t)]'$ decreases in both data sets (Fig. 2). Therefore, as a next step, we identify the range of precipitation rates for which the number of grid points explains at least 50% of the tropical precipitation variability. To do so, we calculate the correlation between the time series of $[P(t)]'$ and of the area fraction of grid points precipitating between 20 mm d^{-1} and a certain threshold (e.g., 20-25 mm d^{-1}, 20-30 mm d^{-1}, 20-35 mm d^{-1}). According to this analysis, 60% of the tropical precipitation variability in ICON-Sapphire (r=0.75) and IMERG (r=0.76) is explained by the changes in the number of grid points precipitating between 20 and 70 mm d^{-1}, $\alpha_{20}^{70}(t)'$ (Table 1). Moreover, the variations in the area fraction of grid points precipitating between 20 and 70 mm d^{-1} match the variations of $[P(t)]'$ in both data sets (Fig. 4). In contrast, the grid points precipitating more than 70 mm d^{-1} have a minor role, even if the correlation with $[P(t)]'$ is high in IMERG (Table 1).

Whereas high precipitation rates do not impact the day-to-day variability in the tropics, one could argue that grid points precipitating less than 20 mm d^{-1} also explain the tropical precipitation variability according to Equation 8. But in this case, the relationship is negative. An increase in the number of points precipitating more than 20 mm d^{-1} means a decrease in the same amount of the number of points precipitating less than 20 mm d^{-1} and an increase in $P(t)'$. The correlation is -0.92 in ICON-Sapphire and -0.92 in IMERG. However, when only including precipitation rates between 0.1 and 20 mm d^{-1}, the correlations between $\alpha_{0.1}^{20}(t)'$ and $[P(t)]'$ is 0.45 in ICON-Sapphire and 0.02 in IMERG, showing that grid points precipitating between 1 and 20 mm d$-$1 do not explain $[P(t)]'$.

Fig. 4

Table 1

Similarly, using other bottom limits than 0.1 mm d^{-1} to approach toward 20 mm d^{-1} (e.g., 1-20 mm d^{-1}, 2-20 mm d^{-1}, ..., 15-20 mm d^{-1}) does not improve the correlation in ICON-Sapphire, which is around 0.3 for all thresholds. But in IMERG, the correlation goes from 0.1 at 1-20 mm d^{-1} to 0.36 at 15-20 mm d^{-1}. Still, the values are much lower than using grid points precipitating between 20 and 70 mm d^{-1}. Therefore, we conclude that the variability in the number of grid points precipitating between 20 and 70 mm d^{-1} strongly influences the tropical precipitation variability (60% of the variability). An hourly precipitation analysis shows that grid points precipitating between 20 and 70 mm d^{-1} tend to precipitate for 5 h in ICON and 7 h in IMERG (Fig. S3). Moreover, those precipitation rates represent 46% and 40% of the mean precipitation in the tropics in ICON-Sapphire and IMERG, respectively (Fig. 1c). Thus, the group of precipitation rates controlling the tropical precipitation variability (20-70 mm d^{-1}) does not have the predominance regarding their contribution to the mean precipitation.

Because precipitation and clouds are intrinsically related, we focus in the next section on identifying the group of clouds accompanying $\alpha_{20}^{70}(t)'$ in ICON-Sapphire.

5. Clouds and the tropical precipitation variability

Distribution of tropical clouds

The distribution of clouds identified according to the method described in section 2 in ICON-Sapphire reveals the expected three peaks related to the three modus of tropical clouds (Fig. 5a). A peak around 2.5 km reflects the predominance of boundary layer cumuli or shallow clouds. The marine stratus clouds located over the eastern side of the Pacific and Atlantic oceans also contribute to the 2.5 km peak. The second peak at 5 km indicates the altitude of the freezing level and the altitude populated by congestus clouds. Finally, a small peak in the distribution of clouds is observed around 10 km due to cumulonimbus. While the distribution of tropical clouds in ICON-Sapphire resembles the distribution using satellite data, the peak related to cumulonimbus clouds is smaller and at a lower altitude compared to satellite estimates (see Fig. 2 in Dessler et al., 2006). A possible explanation for this disparity is the fact of excluding cloud ice in the computation of the cloud height in this study. Fig. 5

ICON-Sapphire shows differences in the cloud distribution between ocean (Fig. 5b) and land (Fig. 5c), and this agrees with observational campaigns over ocean (Rickenbach and Rutledge, 1998; Johnson et al., 1999) and the Amazon (Eissner et al., 2021) which have focused on convective clouds. The distribution of clouds over ocean is similar to the whole tropics due to the large area covered by oceans. But over land, the peak related to boundary layer cumuli increases in altitude by 1 km, maybe related to the more vigorous convection and deeper boundary layer over land. Also, low-level clouds are much less frequent than over ocean, leading to a similar frequency as congestus. The peak related to cumulonimbus is more evident over land than over ocean, meaning that cumulonimbus clouds are relatively more frequent over continents, a feature also observed in satellite data (Liu et al., 2008). Our results indicate an adequate partitioning of the tropical cloud distribution in ICON-Sapphire, but this is not the case for its spatial distribution. ICON-Sapphire shows an overproduction of clouds with CTH less than 2.5 km, in particular over the equatorial region of the Indo-Pacific (not shown). This feature is related to a dry bias present in this region and part of the double ITCZ bias in ICON-Sapphire, as shown in Segura et al. (2022). Table 2

In terms of tropical precipitation, the three types of clouds explain 99.4%

of the total amount of precipitation in the tropics, meaning that omitting ice to classify clouds does not impact our results. Table 2 shows the detailed contribution to the total amount of precipitation and the percentage of the tropical area covered by low-levels clouds, congesti, and cumulonimbi. Low-level clouds cover 60% of the tropics in ICON-Sapphire, but their contribution to the total amount of precipitation is only 8%. In contrast, congesti and cumulonimbi cover 22% and 5%, respectively, of the tropics but contribute 45% and 46%, respectively, to the total precipitation amount. We observe that congesti and cumulonimbi precipitating less than 20 mm d^{-1} equals the contribution of precipitation of congesti and cumulonimbi precipitating more than 70 mm d^{-1} ($\sim$ 24%, Table 2). The fact that tropical clouds with different intensities show a similar precipitation contribution is due to the area they cover from the tropics. Congesti and cumulonimbi precipitating less than 20 mm d^{-1} cover 22.5% of the tropical region while their counterparts precipitating more than 70 mm d^{-1} only 0.8% (Table 2).

Regarding the precipitation rates explaining the precipitation variability (20-70 mm d^{-1}), congesti and cumulonimbi cover a similar area of the tropics ($\sim$ 2%) and have a similar precipitation contribution to the tropical precipitation mean ($\sim$ 20%). Restricting the area to consider only the number of points precipitating between 20 and 70 mm d^{-1}, congesti and cumulonimbi explain 96% of the total amount of precipitation and cover 96%

of the area. Low-level clouds or another type of cloud explains the other 4% of the total amount of precipitation. Thus, congesti or cumulonimbi or both should explain the variation in the number of grid points precipitating between 20 and 70 mm d^{-1} and hence the tropical precipitation variability.

Congesti or cumulonimbi for the precipitation variability?

We quantify for each day the area fraction (with respect to the full tropics) of congestus precipitating between 20 and 70 mm d^{-1}. The area fraction of cumulonimbus precipitating within these precipitation rates is also calculated and displayed in Fig. 6. Fig. 6

A high agreement exists between the time series of the area fraction of congestus precipitating between 20 and 70 mm d^{-1} and $\alpha_{20}^{70}(t)'$ (Fig. 6), with a correlation value of 0.68 (Table 3). This relationship remains after subtracting the seasonal cycle using a running mean of a 60-day time window. The corresponding correlation is then 0.76. Fig. 6 also shows a mismatch of these two times series during boreal spring (March-May). The decrease in the area fraction of congesti precipitating between 20 and 70 mm d^{-1} is stronger than $\alpha_{20}^{70}(t)'$. After excluding the February-May season, the correlation increases from 0.68 to 0.85 (Table 3).

In contrast, the area fraction of cumulonimbi precipitating between 20 and 70 mm d^{-1} weakly correlates with $\alpha_{20}^{70}(t)'$ (r=0.34, Table 3). The correlation does not improve much when using only the period between

June 2020 and January 2021 (r=0.51). The correlation increases when the seasonal cycle is removed (r=0.65), but the value is still lower compared to the one for the congestus clouds. Thus, ICON-Sapphire shows a strong relationship between the area fraction of grid points precipitating between 20 and 70 mm day^{-1} and congestus clouds on seasonal and daily time scales. Table 3

6. Conclusion

This study started with the question of what controls the daily precipitation variability in the tropics. The approach taken was to analyze the tropics as a single entity for which a single time series of daily values of precipitation is calculated. Our purpose in analyzing the daily variations in this time series is to get new insights into how the tropics precipitate on a day-to-day basis and what leads to daily precipitation increase or decrease. Are those light (< 5 mm d^{-1}) or intense (>70 mm d^{-1}) precipitation rates? Or is the change homogeneous throughout precipitation rates? Is the change due to variations in area or intensity? From what type of clouds? And can a global-coupled storm-resolving model reproduce these relationships? To address these questions, we developed a framework to formally derive the contribution from intensity, area, and precipitation rates to the precipitation variability (see Eq. 8). This framework is applied to a one-year simulation of the global-coupled storm-resolving model ICON run with the Sapphire configuration (ICON-Sapphire; Hohenegger et al., 2023) and to observations.

ICON-Sapphire can reproduce important characteristics of the probability density function of precipitation rates. In the simulation and in observations, around 70% of the mean precipitation comes from precipitation rates between 5 and 70 mm d^{-1}. Thus, neither the more frequent precipitation rates (<5 mm d^{-1}) nor the most intense (>70 mm d^{-1}) ones play an important role for the mean precipitation. This already shows the advantage of not using a convective parameterization, in which case the contribution of light precipitation increases to 40-50% of the precipitation mean for the region 50°S-50°N (Dai, 2006).

Concerning the variability of tropical precipitation, we could identify that the daily variations in the number of grid points precipitating between 20 and 70 mm d^{-1} explain 60% of the tropical precipitation variability both in model and observations. Moreover, this relationship does not change if another year in IMERG or another observational data set is selected. Removing the seasonal cycle confirms that the variability in the area covered by precipitation rates between 20 and 70 mm d^{-1} explains 60% of the tropical precipitation variability. Our results also highlight that the group of precipitation rates controlling the precipitation variability in the tropics is not the same one as controlling the mean. Precipitation rates between 20 and 70 mm d^{-1} only contribute to 46% of the tropical precipitation mean in ICON-Sapphire and 40% in IMERG.

The identification of the precipitation rates explaining the day-to-day variations in tropical precipitation allowed us to answer the question of which type of convective clouds (low-level, congestus, or cumulonimbus) are responsible for those precipitation rates in ICON-Sapphire. Congestus and cumulonimbus are equally important for tropical precipitation in ICON-Sapphire, around 45% of the total tropical precipitation comes from each one. This is also the case when reducing the domain to regions precipitating between 20 and 70 mm d^{-1}. Differently, the daily variation in the number of grid points precipitating between 20 and 70 mm d^{-1} is related to congestus clouds (r=0.68). This relationship gets stronger when avoiding the boreal spring (February 2020 - May 2020). In contrast, the number of grid points with cumulonimbus clouds has a weak influence. The correlation is 0.3 considering the whole period (February 2020 to January 2021) and 0.4 when avoiding the boreal spring season.

Acknowledgements

This work is supported by the Hans-Ertel Centre for Weather Research (project number 4818DWDP1A), which funded H. Segura, and by the European Union's Horizon 2020 research and innovation program project NextGEMS (grant agreement number 101003470), which funded C. Hohenegger. The European Horizon 2020 project CONSTRAIN (project number 493B) also financed this work with the project number 493B. Compute time was provided by DKRZ under projects bm1235 and bb1153. The authors also thank Jin-Song von Storch for her comments during the internal revision. Discussions with Christian Jakob at the early stage of this work are also acknowledged. We also thank the two anonymous reviewers for their constructive comments.

Data Availability Statement

The ICON branch nextgems_cycle1 _dpp0066 (commit 62dbfc) was used to obtain the ICON-Sapphire simulation. The source code of ICON is available to individuals under licenses (`https://mpimet.mpg.de/en/science/modeling-with-icon/code-availability`) and can be downloaded where `https://doi.org/10.17617/3.1XTSR6`. We use IMERG data ((Huffman et al., 2019)) from the Integrated Climate Data Center website `https://www.cen.uni-hamburg.de/en/icdc/data/ocean/hadisst1.html`. Scripts used for the analysis can be found in `https://gitlab.dkrz.de/m300876/clouds_precipitation.git`

References

Atlas, D., D. Rosenfeld, and D. A. Short, 1990: The estimation of convective rainfall by area integrals: 1. The theoretical and empirical basis. *J. Geophys. Res. Atmos.*, **95(D3)**, 2153–2160.

Berndtsson, R., and J. Niemczynowicz, 1988: Spatial and temporal scales in rainfall analysis — Some aspects and future perspectives. *J. Hydrol.*, **100(1)**, 293–313.

Cabas, J., A. Weersink, and E. Olale, 2010: Crop yield response to economic, site and climatic variables. *Clim. Change*, **101(3)**, 599–616.

Cheng, C.-P., and R. A. Houze, 1979: The Distribution of Convective and Mesoscale Precipitation in GATE Radar Echo Patterns. *Mon. Weather Rev.*, **107(10)**, 1370–1381.

Cristiano, E., M.-C. ten Veldhuis, and N. van de Giesen, 2017: Spatial and temporal variability of rainfall and their effects on hydrological response in urban areas – a review. *Hydrol. Earth Syst. Sci.*, **21(7)**, 3859–3878.

Da Silva, N. A., B. G. Webber, A. J. Matthews, M. M. Feist, T. H. Stein, C. E. Holloway, and M. F. Abdullah, 2021: Validation of GPM IMERG Extreme Precipitation in the Maritime Continent by Station and Radar Data. *Earth Sp. Sci.*, **8(7)**, 1–18.

Dai, A., 2006: Precipitation characteristics in eighteen coupled climate models. *J. Clim.*, **19(18)**, 4605–4630.

Dessler, A. E., S. P. Palm, and J. D. Spinhirne, 2006: Tropical cloud-top height distributions revealed by the Ice, Cloud, and Land Elevation Satellite (ICESat)/Geoscience Laser Altimeter System (GLAS). *J. Geophys. Res. Atmos.*, **111(12)**, 1–11.

Doneaud, A., S. Ionescu-Niscov, D. L. Priegnitz, and P. L. Smith, 1984: The Area-Time Integral as an Indicator for Convective Rain Volumes. *J. Appl. Meteorol. Climatol.*, **23(4)**, 555–561.

Eissner, J. M., D. B. Mechem, M. P. Jensen, and S. E. Giangrande, 2021: Factors Governing Cloud Growth and Entrainment Rates in Shallow Cumulus and Cumulus Congestus During GoAmazon2014/5. *J. Geophys. Res. Atmos.*, **126(12)**, 1–16.

Fang, J., W. Yang, Y. Luan, J. Du, A. Lin, and L. Zhao, 2019: Evaluation of the TRMM 3B42 and GPM IMERG products for extreme precipitation analysis over China. *Atmos. Res.*, **223(March)**, 24–38.

Fiedler, S., T. Crueger, R. D'Agostino, K. Peters, T. Becker, D. Leutwyler, L. Paccini, J. Burdanowitz, S. A. Buehler, A. U. Cortes, T. Dauhut, D. Dommenget, K. Fraedrich, L. Jungandreas, N. Maher, A. K.

Naumann, M. Rugenstein, M. Sakradzija, H. Schmidt, F. Sielmann, C. Stephan, C. Timmreck, X. Zhu, and B. Stevens, 2020: Simulated tropical precipitation assessed across three major phases of the coupled model intercomparison project (CMIP). *Mon. Weather Rev.*, **148(9)**, 3653–3680.

Hohenegger, C., P. Korn, L. Linardakis, R. Redler, R. Schnur, P. Adamidis, J. Bao, S. Bastin, M. Behravesh, M. Bergemann, J. Biercamp, H. Bockelmann, R. Brokopf, N. Brüggemann, L. Casaroli, F. Chegini, G. Datseris, M. Esch, G. George, M. Giorgetta, O. Gutjahr, H. Haak, M. Hanke, T. Ilyina, T. Jahns, J. Jungclaus, M. Kern, D. Klocke, L. Kluft, T. Kölling, L. Kornblueh, S. Kosukhin, C. Kroll, J. Lee, T. Mauritsen, C. Mehlmann, T. Mieslinger, A. K. Naumann, L. Paccini, A. Peinado, D. S. Praturi, D. Putrasahan, S. Rast, T. Riddick, N. Roeber, H. Schmidt, U. Schulzweida, F. Schütte, H. Segura, R. Shevchenko, V. Singh, M. Specht, C. C. Stephan, R. Vogel, C. Wengel, M. Winkler, F. Ziemen, J. Marotzke, and B. Stevens, 2023: ICON-Sapphire : simulating the components of the Earth System and their interactions at kilometer and subkilometer scales. *Geosci. Model Dev.* 779–811.

Houze, R. A., and C.-P. Cheng, 1977: Radar Characteristics of Tropical

Convection Observed During GATE: Mean Properties and Trends Over the Summer Season. *Mon. Weather Rev.*, **105(8)**, 964–980.

Huffman, G., E. Stocker, D. Bolvin, E. Nelkin, and J. Tan, 2019: , GPM IMERG Final Precipitation L3 Half Hourly 0.1 degree x 0.1 degree V06. Technical report, Greenbelt, MD, Goddard Earth Sciences Data and Information Services Center (GES DISC),[last access: February 26, 2022], distributed in netCDF file format by ICDC, CEN, University of Hamburg.

Johnson, R. H., T. M. Rickenbach, S. A. Rutledge, P. E. Ciesielski, and W. H. Schubert, 1999: Trimodal characteristics of Tropical convection. *J. Clim.*, **12(8 PART 1)**, 2397–2418.

Judt, F., and R. Rios-Berrios, 2021: Resolved Convection Improves the Representation of Equatorial Waves and Tropical Rainfall Variability in a Global Nonhydrostatic Model. *Geophys. Res. Lett.*, **48(14)**, 1–10.

Liu, C., E. J. Zipser, D. J. Cecil, S. W. Nesbitt, and S. Sherwood, 2008: A cloud and precipitation feature database from nine years of TRMM observations. *J. Appl. Meteorol. Climatol.*, **47(10)**, 2712–2728.

Lopez, R. E., D. O. Blanchard, R. L. Holle, J. L. Thomas, D. Atlas, and D. Rosenfeld, 1989: Estimation of Areal Rainfall Using the Radar

Echo Area Time Integral. *J. Appl. Meteorol. Climatol.*, **28(11)**, 1162–1175.

Ma, H. Y., S. A. Klein, J. Lee, M. S. Ahn, C. Tao, and P. J. Gleckler, 2022: Superior Daily and Sub-Daily Precipitation Statistics for Intense and Long-Lived Storms in Global Storm-Resolving Models. *Geophys. Res. Lett.*, **49(8)**.

Moon, H., L. Gudmundsson, B. P. Guillod, V. Venugopal, and S. I. Seneviratne, 2019: Intercomparison of daily precipitation persistence in multiple global observations and climate models. *Environ. Res. Lett.*, **14(10)**.

Mukabutera, A., D. Thomson, M. Murray, P. Basinga, L. Nyirazinyoye, S. Atwood, K. P. Savage, A. Ngirimana, and B. L. Hedt-Gauthier, 2016: Rainfall variation and child health: Effect of rainfall on diarrhea among under 5 children in Rwanda, 2010. *BMC Public Health*, **16(1)**, 1–9.

Na, Y., Q. Fu, and C. Kodama, 2020: Precipitation Probability and Its Future Changes From a Global Cloud-Resolving Model and CMIP6 Simulations. *J. Geophys. Res. Atmos.*, **125(5)**, 1–23.

Pendergrass, A. G., R. Knutti, F. Lehner, C. Deser, and B. M. Sanderson, 2017: Precipitation variability increases in a warmer climate. *Sci. Rep.*, **7(1)**, 1–9.

Rickenbach, T. M., and S. A. Rutledge, 1998: Convection in TOGA COARE: Horizontal scale, morphology, and rainfall production. *J. Atmos. Sci.*, **55(17)**, 2715–2729.

Roehrig, R., D. Bouniol, F. Guichard, F. déric Hourdin, and J. L. Redelsperger, 2013: The present and future of the west african monsoon: A process-oriented assessment of CMIP5 simulations along the AMMA transect. *J. Clim.*, **26(17)**, 6471–6505.

Rowhani, P., D. B. Lobell, M. Linderman, and N. Ramankutty, 2011: Climate variability and crop production in Tanzania. *Agric. For. Meteorol.*, **151(4)**, 449–460.

Segura, H., C. Hohenegger, C. Wengel, and B. Stevens, 2022: Learning by Doing: Seasonal and Diurnal Features of Tropical Precipitation in a Global-Coupled Storm-Resolving Model. *Geophys. Res. Lett.*, **49(24)**, 1–10.

Shively, G. E., 2017: Infrastructure mitigates the sensitivity of child growth to local agriculture and rainfall in Nepal and Uganda. *Proc. Natl. Acad. Sci. U. S. A.*, **114(5)**, 903–908.

Sun, Q., C. Miao, Q. Duan, H. Ashouri, S. Sorooshian, and K. L. Hsu, 2018: A Review of Global Precipitation Data Sets: Data Sources, Estimation, and Intercomparisons. *Rev. Geophys.*, **56(1)**, 79–107.

Tan, J., W. A. Petersen, and A. Tokay, 2016: A novel approach to identify sources of errors in IMERG for GPM ground validation. *J. Hydrometeorol.*, **17(9)**, 2477–2491.

Warner, C., J. Simpson, G. V. Helvoirt, D. W. Martin, D. Suchman, and G. L. Austin, 1980: Deep Convection on Day 261 of GATE. *Mon. Weather Rev.*, **108(2)**, 169–194.

Wen, Y., A. Behrangi, H. Chen, and B. Lambrigtsen, 2018: How well were the early 2017 California Atmospheric River precipitation events captured by satellite products and ground-based radars? *Q. J. R. Meteorol. Soc.*, **144(January)**, 344–359.

Zhang, A., L. Xiao, C. Min, S. Chen, M. Kulie, C. Huang, and Z. Liang, 2019: Evaluation of latest GPM-Era high-resolution satellite precipitation products during the May 2017 Guangdong extreme rainfall event. *Atmos. Res.*, **216(May 2018)**, 76–85.

Zhou, Y., W. K. M. Lau, and C. Liu, 2013: Rain characteristics and large-scale environments of precipitation objects with extreme rain volumes from TRMM observations. *J. Geophys. Res. Atmos.*, **118(17)**, 9673–9689.

List of Figures

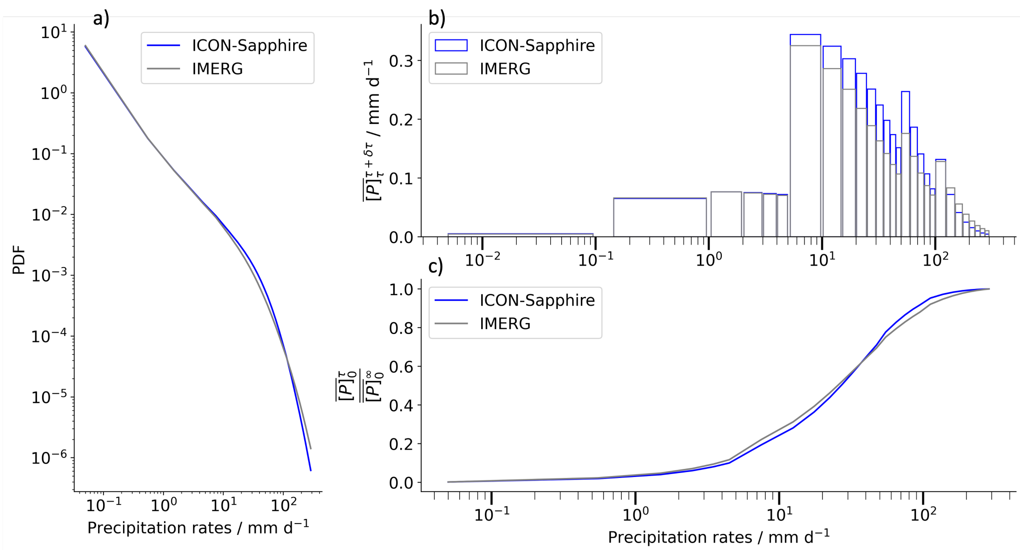

Fig. 1. Tropical precipitation distribution for ICON-Sapphire (blue) and IMERG (grey) using daily values between February 2020 and January 2021. a) Normalized distribution of precipitation rates. b) Precipitation mean of individual bins (Equation 1). c) Cumulative precipitation obtained from b). The tropics are considered from 30°S and 30°N

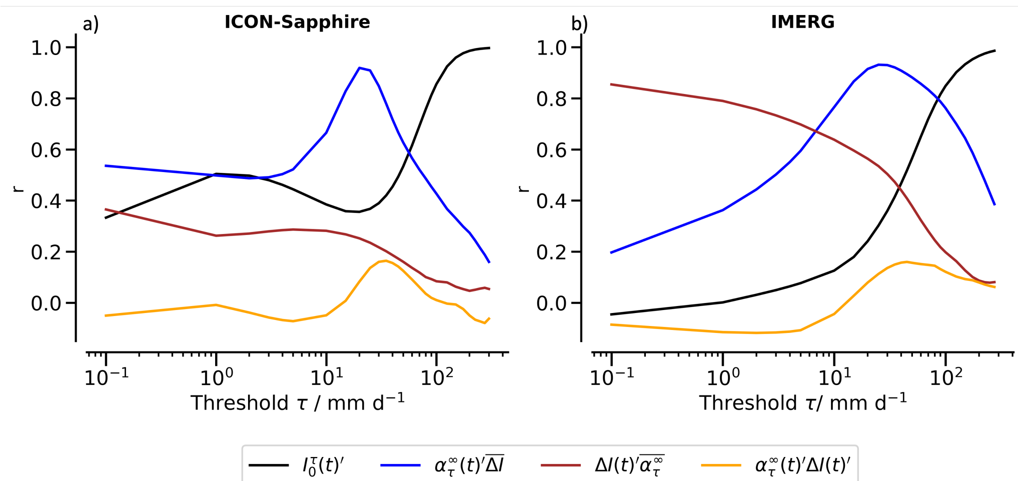

Fig. 2. Correlation values (r) between the time series of tropical precipitation variability ($[P(t)]'$) and the time series of the terms in Equation 8 with time-dependent components. The evaluation is done for different precipitation thresholds τ (x-axis). a) for ICON-Sapphire and b) for IMERG.

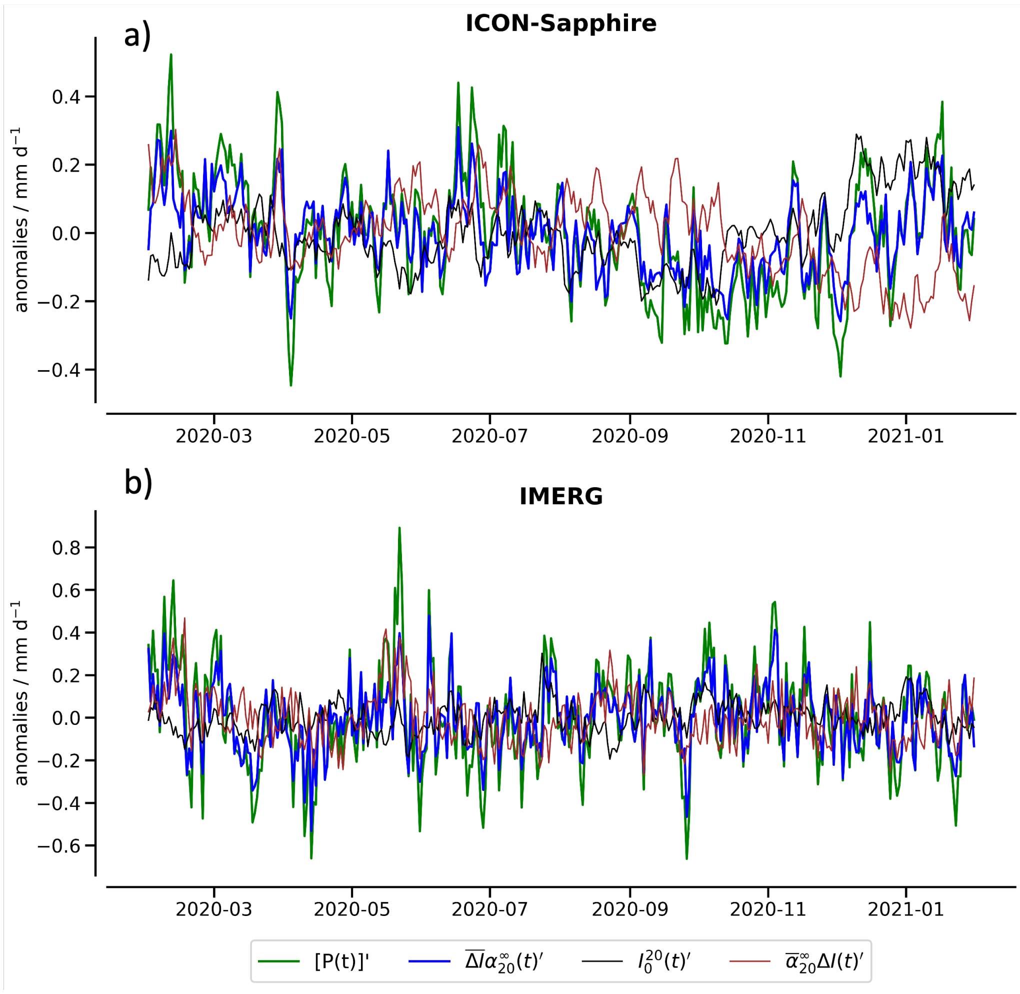

Fig. 3. Time series of the terms with time-dependent component in Equation 8 when using a precipitation threshold of 20 mm d^{-1}.

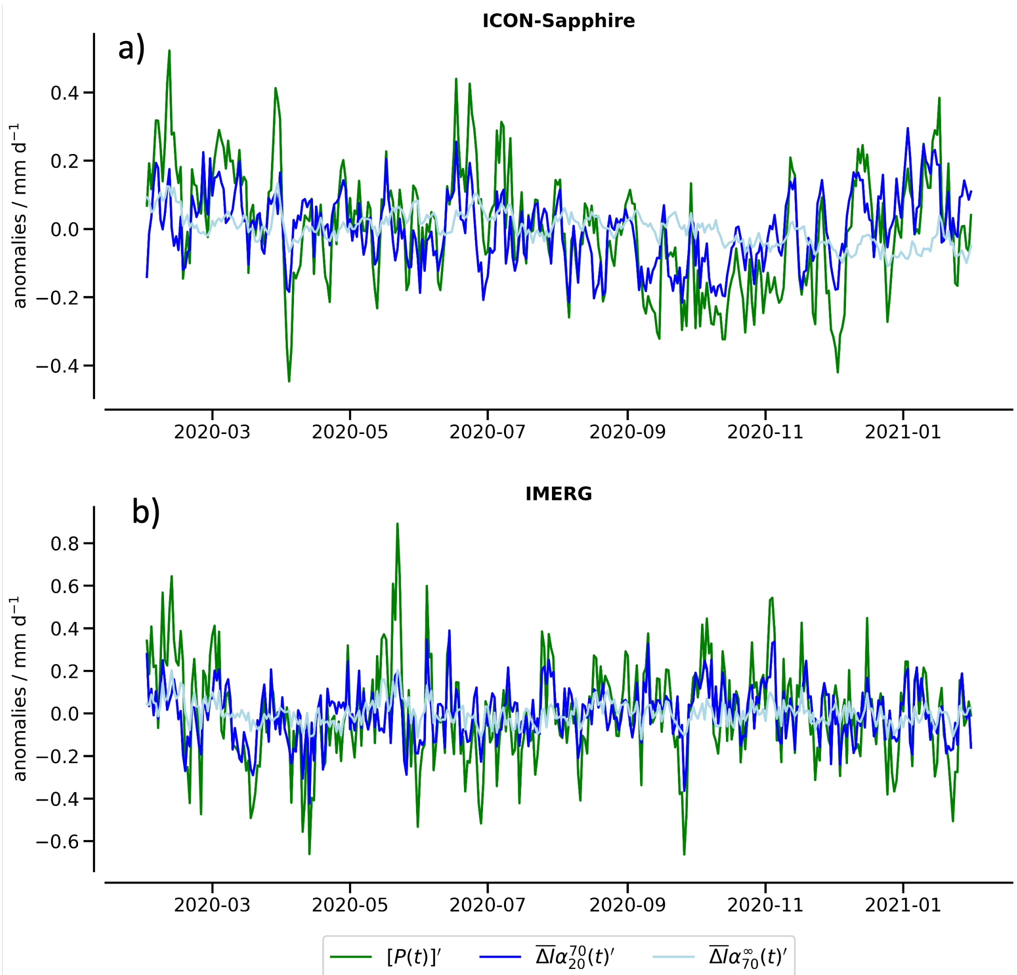

Fig. 4. Similar to Fig. 3, but showing the temporal variation in the area fraction of precipitation rates between 20 and 70 mm d^{-1} ($\alpha_{20}^{70}(t)'$, blue line) and greater than 70 mm d^{-1} ($\alpha_{70}^{\infty}(t)'$, orange line). $\overline{\Delta I}$ is the difference between $\overline{\Delta I_2 0^{\infty}}$ and $\overline{\Delta I_0^{20}}$.

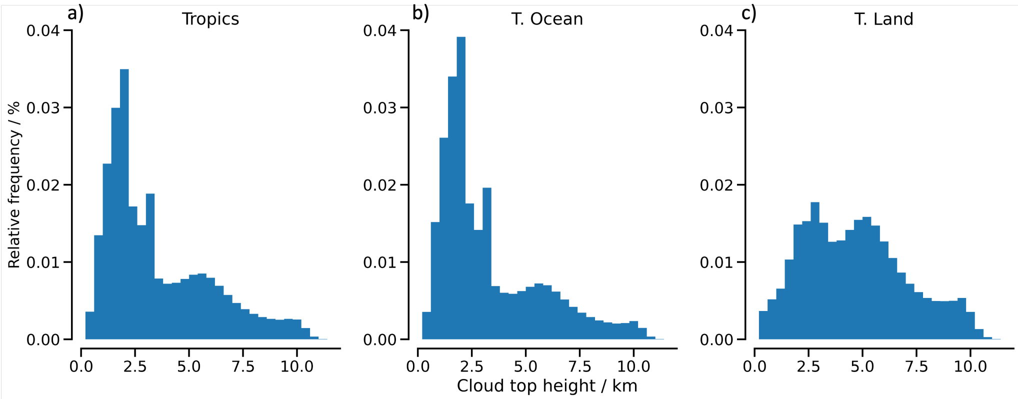

Fig. 5. Normalized distribution of cloud top height in ICON-Sapphire. a) All the tropics, b) tropical ocean and c) tropical land. The method of calculation is explained in section 2.

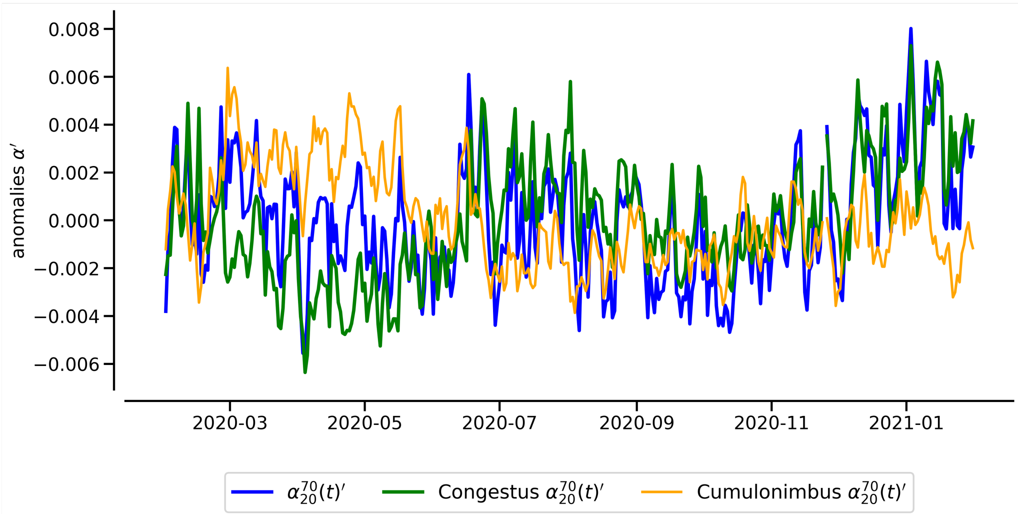

Fig. 6. Time variation in the area fraction of precipitation rates between 20 and 70 mm d^{-1} ($\alpha_{20}^{70}(t)'$,blue line). The time variation in the number of grid points with congestus and cumulunimbus clouds precipitating between 20 and 70 mm d^{-1} are displayed as a green and orange line, respectively.

List of Tables

Table 1. Correlation between the time series of tropical precipitation variability ($[P(t)]'$) and of the area fraction of grid points precipitating more than 20mm d^{-1} ($\alpha_{20}^{\infty}(t)'$), between 20 and 70 mm d^{-1} ($\alpha_{20}^{70}(t)'$) and more than 70 mm d^{-1} ($\alpha_{70}^{\infty}(t)'$) in ICON-Sapphire and IMERG. Deseasonal correlation is computed after removing the seasonal variability by using a running mean with a 60-day window.

	ICON-Sapphire			IMERG		
	$\alpha_{20}^{\infty}(t)'$	$\alpha_{20}^{70}(t)'$	$\alpha_{70}^{\infty}(t)'$	$\alpha_{20}^{\infty}(t)'$	$\alpha_{20}^{70}(t)'$	$\alpha_{70}^{\infty}(t)'$
Correlation	0.92	0.75	0.52	0.92	0.76	0.83
Deseasonal correlation	0.90	0.76	0.59	0.90	0.75	0.81

Table 2. Area covered and precipitation contribution in the tropics from low-level, congestus and cumulonimbus clouds classified according to the cloud top height (CTH; see section 2). Only clouds with a base height lower than 3km are considered for the analysis. The numbers inside the parenthesis represent the partition regarding three precipitating regions, less than 20 mm d^{-1} (first number), between 20 and 70 mm d^{-1} (second number) and more than 70 mm d^{-1} (third number).

Cloud type	Cloud top height (CTH) /km	Area covered /%	Precipitation contribution /%
Low-level clouds	CTH<4km	59.5 (59.3 / 0.1 / 0)	8 (6.8 / 1.1/ 0.2)
Congestus	4km $\leq$ CTH<8km	22.5 (20.0 / 2.25 / 0.2)	45.1 (18.7 / 20.7 / 5.8)
Cumulonimbus	8km $\leq$ CTH<15km	5.2 (2.5 / 2.1 / 0.6)	46.3 (4.9 / 22.4 / 18.7)

Table 3. Correlation between the time series of the area fraction of grid points precipitating between 20 and 70 mm d^{-1} ($\alpha_{20}^{70}(t)'$) and of the area fraction of congestus and cumulonimbus clouds precipitating between 20 and 70 mm d^{-1}. Deseasonal correlation is computed after removing the seasonal variability by using a running mean with a 60-day window.

	February 2020 to January 2021		June 2020 to January 2021	
	Congestus	Cumulonimbus	Congestus	Cumulonimbus
Correlation	0.68	0.34	0.85	0.51
Deseasonal correlation	0.76	0.65	0.8	0.64